The strength of tumor reactivity is uncoupled from clonal expansion among TIL-derived TCRs

Shian Ouyang# [1], Zihan Zhao# [1, 2], Siyang Liu[2], Shichen Ma[1], Xiangyu Wu[2], Mingxin Fan[1], Ning Jiang[2], Rong Yang[2], Jie P. Li* [1]

1. State Key Laboratory of Coordination Chemistry, Chemistry and Biomedicine Innovation Center (ChemBIC), School of Chemistry, Nanjing University, Nanjing 210033, China;
2. Department of Urology, Affiliated Drum Tower Hospital, Medical School of Nanjing University, Nanjing 210008, China;

# These authors contributed equally.

* Corresponding author: jieli@nju.edu.cn

Abstract

Highly expanded clonotypes are widely used to enrich tumor-reactive TCRs, yet expansion may not faithfully report functional reactivity. Using direct tumor-cell recognition as the benchmark, we found that in native E0771 and LLC tumors, highly expanded clonotypes did not consistently show the strongest responses, whereas reactive TCRs were also present among low-frequency clones. We next used the antigen-controlled MB49-OVA model to jointly measure TCR functional avidity, peptide–MHC presentation abundance and tumor-cell recognition. In this setting, TCRs with different avidities for the same antigen could converge to similar expansion levels in vivo. Moreover, peptide–MHC presentation abundance was sufficient to reshape the reactivity hierarchy predicted from avidity alone, and distinct avidity–presentation combinations were linked to biased transcriptional states. Thus, clonal expansion is a context-dependent enrichment cue rather than a stable surrogate of tumor reactivity, and low-frequency clonotypes may provide a valuable reservoir for tumor-reactive TCR discovery.

Introduction

Tumor-infiltrating lymphocyte (TIL)-based therapies and engineered TCR-T cell therapies both rely on the identification of T cells or TCRs that can directly recognize tumor targets and mediate antitumor activity (1, 2). In practice, however, nominating such tumor-reactive TCRs from polyclonal TIL repertoires remains a major bottleneck (3–5). Because only a limited number of candidate TCRs can usually be reconstructed and functionally tested, most workflows rely on indirect prioritization rules to enrich for clonotypes that are more likely to be reactive (6–8).

Among these, clonal expansion is one of the most widely used heuristics, based on the premise that antigen-driven T cells should preferentially accumulate in tumors through activation and proliferation (6). This strategy provides a practical entry point for candidate selection, but whether clone size can reliably reflect functional tumor reactivity across tumor contexts remains unclear. Native tumors contain highly heterogeneous T cell populations, including bystander clonotypes whose infiltration or expansion is not necessarily maintained by ongoing tumor-antigen recognition (3, 9). Moreover, even for truly tumor-reactive clonotypes, clonal expansion reflects a cumulative population outcome over time rather than an immediate measurement of ongoing tumor-cell recognition (10, 11). As a result, clonotype frequency may enrich candidate tumor-reactive TCRs in

some settings, yet still fail to indicate which clonotypes mediate the strongest tumor recognition.

Accordingly, when clone size fails to stably explain functional differences among reactive TCRs, attention needs to shift to variables that more directly influence tumor-cell recognition. Mechanistically, T cell activation integrates signal 1 (TCR–pMHC), signal 2 (co-stimulation/co-inhibition) and signal 3 (cytokines/inflammation) (12). Because direct tumor recognition fundamentally depends on signal 1, two variables are particularly relevant: the intrinsic affinity of a TCR for its cognate peptide–MHC complex, and the abundance with which that peptide is presented on tumor cells (13, 14). Although this principle is conceptually well appreciated, these two variables are rarely resolved together for functionally validated tumor-reactive clonotypes in native tumors (4, 15). As a result, while we may identify which TCRs are tumor-reactive, it remains difficult to determine to what extent functional differences among reactive TCRs are jointly constrained by avidity and peptide presentation abundance.

Here, we use direct tumor-cell recognition as the reference criterion for tumor reactivity and first test how well clonal expansion captures this property in native tumor models. In E0771 and LLC, we combine paired scRNA-seq/scTCR-seq with clonotype-level functional validation to examine the relationship between tumor reactivity and clone size. We then use the antigen-controlled MB49-OVA system to jointly quantify TCR functional avidity, peptide presentation abundance and tumor-cell recognition strength within the same framework. This design allows us to ask whether tumor reactivity is better understood through the combined effects of avidity and peptide presentation than through clone size alone, and whether distinct avidity–presentation combinations are associated with distinct transcriptional state biases in vivo.

Materials and methods

Cell lines

Unless otherwise noted, all cell lines used in this study were obtained from ATCC. E0771, LLC, MB49, MB49-OVA, and Jurkat-derived cell lines were cultured in RPMI 1640 medium (Gibco) supplemented with 10% fetal bovine serum (FBS; Gibco), 100 IU/mL penicillin, and 100 μg/mL streptomycin. HEK293T cells were maintained in DMEM (Gibco) containing 10% FBS, 100 IU/mL penicillin, and 100 μg/mL streptomycin. TCR-transduced Jurkat cell lines were established by lentiviral transduction of ΔTCR Jurkat cells (ATCC, J.RT3-T3.5). MB49-OVA cells were derived from parental MB49 cells by lentiviral transduction. All cells were maintained at 37°C in a humidified incubator with 5% CO_2.

Mice and tumor models

Specific pathogen-free (SPF) C57BL/6J male mice (6–8 weeks old) were purchased from GemPharmatech (Nanjing, China) and housed under SPF conditions. All animal experiments were approved by the Animal Ethics and Welfare Committee (AEWC; Approval No. IACUC-2012003). For tumor implantation, subcutaneous tumor models were established using E0771, LLC, MB49-OVA, or MB49 cells. Tumor cells were prepared at 1.5×10^7 cells/mL in a mixture of Ceturegel Matrix LDEV-Free (Yeasen) and DPBS, with one part matrix to four parts DPBS. Each mouse received a subcutaneous injection of 100 μL of the cell suspension. Tumors were harvested when they reached approximately 800 mm^3.

Flow cytometry and cell sorting

For flow cytometric analysis, cells were first incubated with Fc blocking reagent (BioLegend) and Zombie Aqua™ (BioLegend) at room temperature for 10 min, followed by surface staining with the indicated antibody panel on ice for 30 min. After staining, cells were washed twice with FACS buffer consisting of DPBS supplemented with 2% FBS and 1 mM EDTA (Gibco). Flow cytometry data were acquired on an Agilent NovoCyte Quantum and analyzed accordingly. For sorting experiments, stained cells were washed twice with FACS buffer and sorted on a BD FACSAria III sorter. Unless otherwise indicated, antibodies used in this study were purchased from BioLegend.

Preparation of $CD8^+$ TILs

Freshly isolated tumors were mechanically dissociated and filtered through a 70-μm cell strainer to generate single-cell suspensions. After red blood cell lysis, cells were incubated with Fc blocking reagent and stained with anti-mCD45-AF700 (clone 30-F11), anti-mCD3-PE (clone 17A2), anti-mCD8-APC (clone 53-6.7), and Zombie Aqua™. Live $CD45^+CD3^+CD8^+$ tumor-infiltrating lymphocytes were purified by fluorescence-activated cell sorting. Sorted TILs were cultured in RPMI 1640 supplemented with 10% FBS, 1 mM sodium pyruvate (Gibco), 50 μM β-mercaptoethanol (Gibco), 10 mM HEPES (Gibco), 1× MEM NEAA (Gibco), 100 IU/mL penicillin (Gibco), 100 μg/mL streptomycin (Gibco), IL-2 (3,000 IU/mL, T&L Biological Technology, Beijing, China), and anti-mCD3 antibody (30 ng/mL, BioXCell) before downstream assays.

Proximity-labeling-guided prioritization of candidate tumor-reactive clonotypes

To enrich candidate tumor-reactive clonotypes, we adapted previously reported intercellular proximity-labeling strategies into a screening workflow (16–18). Briefly, tumor cells were incubated with 0.05 mg/mL 1,3-fucosyltransferase (1,3-FT) and 10 μM GDP-fucose-$Ru(bpy)_3^{2+}$ on ice for 20 min (17), washed twice with PBS, and resuspended in FACS buffer. The labeled tumor cells were then co-incubated with the corresponding $CD8^+$ TILs for 2 h. Biotin-PEG_3-hydrazide (CAS: 1381861-94-4, Confluore, Xi'an, China) was added at a final concentration of 100 μM, and the cell mixtures were irradiated with 450-nm light for 5 min to initiate proximity-dependent labeling. After three washes with FACS buffer, cells were stained on ice for 30 min with an ssDNA-conjugated streptavidin reagent and sorted for paired single-cell RNA/TCR sequencing (19). Single-cell capture, reverse transcription, and library construction were performed on the Singleron Matrix® platform using the sCircle™ Single Cell Full-Length Immunoreceptor Library Kit (Singleron Biotechnologies, Nanjing, China) according to the manufacturer's instructions. Labeling-associated signals were considered during candidate selection for TCR reconstruction and functional validation.

Processing of scTCR-seq data and clonotype definition

scTCR-seq reads were processed using the CeleScope pipeline with a V(D)J reference based on refdata-cellranger-vdj-GRCm38-alts-ensembl-5.0.0. Filtered TCR contig annotations were imported into R for downstream analysis. TCR clonotypes were defined by paired CDR3 amino acid sequences of the α and β chains. Cells with only one productive chain were retained as independent clonotypes and were not merged with dual-chain clonotypes sharing the same α or β CDR3 sequence. Clonotype size was defined as the number of cells assigned to each clonotype. For clonotype-level analyses, only clonotypes represented by at least five cells were included unless otherwise indicated.

Single-cell transcriptomic analysis

Raw scRNA-seq data were processed using the CeleScope pipeline and aligned to the mouse reference genome mm10 to generate gene expression matrices. Downstream analyses were

performed in R using Seurat (v 5.4.0), dplyr (v 1.2.1), ggplot2 (v 4.0.2), pheatmap (v 1.0.13), harmony (v 1.2.4) and ggpubr (v 0.6.3). For each dataset, cells with fewer than 200 detected genes, more than 5,000 detected genes, or more than 5% mitochondrial transcripts were excluded. Gene expression values were normalized using the LogNormalize method with a scale factor of 10,000. The top 2,000 highly variable genes were identified using the FindVariableFeatures function with the "vst" method. The data were then scaled using all genes, followed by principal component analysis. Shared nearest-neighbor graph construction, clustering, and UMAP visualization were performed using the first 20 principal components with the FindNeighbors, FindClusters, and RunUMAP functions, respectively. Clustering was performed at a resolution of 0.5. Cell subsets were manually annotated according to canonical marker genes, as shown in Fig. S2I.

Functionally validated TCR clonotypes were mapped back to the single-cell atlas according to their paired CDR3α–CDR3β identifiers. Cells carrying validated clonotypes were highlighted on UMAP plots to examine their distribution across transcriptional subsets. For clonotype-level composition analysis, the number and proportion of cells from each validated clonotype falling into each annotated transcriptional subset were calculated based on single-cell annotations. For group-level analyses, validated clonotypes were further assigned to functional groups according to peptide specificity, functional avidity, or tumor-cell recognition properties, and the distribution of each group across transcriptional subsets was quantified.

Differential gene-expression analysis among validated TCR groups was performed using the FindMarkers function in Seurat. For comparisons among SIIN_High, SIIN_Low, and KVV groups, cells carrying validated TCRs were first assigned to the corresponding epitope/avidity group. Each group was then compared against the other two groups using FindMarkers with only.pos = TRUE, logfc.threshold = 0.25, and min.pct = 0.1. Top differentially expressed genes were selected based on expression frequency and average log2 fold change and visualized using DotPlot. Dot color represents scaled average expression, and dot size represents the percentage of cells expressing each gene.

For integrated analysis of parental MB49 and MB49-OVA $CD8^+$ TILs, the two Seurat objects were first processed by SCTransform separately and then merged. Sample identity was recorded as "MB49 $CD8^+$ TILs" or "MB49_OVA CD8 TILs" and used as the batch variable for integration. The top 3,000 integration features were selected using SelectIntegrationFeatures. Principal component analysis was performed on the selected features, and Harmony correction was then applied to the PCA embeddings using sample identity as the grouping variable. Harmony-corrected embeddings were used for downstream UMAP visualization, shared nearest-neighbor graph construction, and clustering. Specifically, the first 30 Harmony dimensions were used for RunUMAP, FindNeighbors, and FindClusters, with a clustering resolution of 0.5. For selected marker genes, violin plots were generated using log-normalized RNA expression values from the RNA assay. *P* values shown on violin plots were calculated by two-sided Wilcoxon rank-sum tests across cells.

Plasmid cloning and construction

TCR constructs encoding the α and β chains linked by a P2A peptide were synthesized by Genecfps (Wuxi, China) and cloned into the lentiviral vector pLV (Addgene no. 36084) for lentiviral production.

Lentiviral production and transduction

For lentiviral production, HEK293T cells were seeded in 10-cm dishes and transfected with the transfer vector together with pMD2.G (Addgene no. 12259), pRSV-Rev (Addgene no. 12253), and pMDLg/pRRE (Addgene no. 12251) using PEI in Opti-MEM. For each dish, 5.625 μg transfer vector, 1.875 μg pMD2.G, 4.5 μg pRSV-Rev, 4.5 μg pMDLg/pRRE, and 50 μg PEI were used in a total volume of 1 mL. The medium was replaced 8 h after transfection. Viral supernatants were collected 48 h later, filtered through a 0.45-μm membrane, aliquoted, and stored at −80°C until use.

For Jurkat transduction, 3×10^5 ΔTCR Jurkat cells were incubated with 150 μL lentiviral supernatant in a 24-well plate in the presence of polybrene (Beyotime Biotechnology) at a final concentration of 8 μg/mL, and the total volume was adjusted to 600 μL with culture medium. Cells were centrifuged at 1,000 × g for 90 min at 32°C and then cultured for an additional 18 h. The viral medium was subsequently replaced with fresh medium. TCR expression was analyzed 2 days later by flow cytometry using anti-mouse TCRβ chain-PE (clone H57-597).

Jurkat-based tumor-cell recognition assay

For functional validation of candidate TCRs, TCR-transduced Jurkat cells were co-cultured with the corresponding tumor cell lines at a 1:2 ratio for 18 h, and T cell activation was assessed by CD69 induction. Before co-culture, tumor cells were labeled with CFSE (Thermo Fisher) at a final concentration of 1 μM for 20 min at room temperature and then washed three times with FACS buffer to enable discrimination from Jurkat cells during flow cytometric analysis. After co-culture, cells were stained with anti-mouse TCRβ chain-PE and anti-hCD69-APC (clone FN50). CD69 induction in Jurkat cells was quantified by flow cytometry. The gating strategy is shown in Fig. S1D.

Peptide stimulation assay and functional avidity analysis

To assess peptide sensitivity, TCR-transduced Jurkat cells were co-cultured with H-2K^b-expressing MC38 cells at a 1:2 ratio for 18 h in the presence of serially diluted SIINFEKL or KVVRFDKL (Synpeptide, Nanjing, China) peptide at final concentrations ranging from 10^{-12} to 10^{-5} mol/L. MC38 cells were pre-labeled with CFSE as described above. After co-culture, cells were stained with anti-mouse TCRβ chain-PE and anti-CD69-APC, and Jurkat activation was quantified as the frequency of CD69$^+$ cells by flow cytometry. Dose–response curves were generated on the basis of CD69 induction, and EC_{50} values were calculated accordingly.

MHC-I immunopeptidomics of MB49-OVA

For immunopeptidomics analysis, MB49-OVA cells were lysed in IP lysis buffer (Thermo Fisher Scientific) supplemented with protease inhibitor cocktail (cOmplete™, EDTA-free, Sigma-Aldrich) and Benzonase nuclease (Merck). Lysates were clarified by centrifugation at 20,000 × g for 90 min at 4°C, and the supernatants were collected for immunoprecipitation. Anti-H-2K^b monoclonal antibody Y3 (BioXCell) was coupled to Protein G Dynabeads (Invitrogen) and crosslinked in 0.2 M sodium borate buffer (pH 9.0) containing freshly prepared 20 mM dimethyl pimelimidate, followed by quenching with 50 mM Tris-HCl (pH 8.0). After washing with PBS, the antibody-coupled beads were incubated with clarified lysates for 2 h at room temperature with gentle rotation. Beads were then washed sequentially with 150 mM NaCl in 20 mM Tris-HCl (pH 8.0), 400 mM NaCl in 20 mM Tris-HCl (pH 8.0), and 20 mM Tris-HCl (pH 8.0). MHC-I-bound peptides were eluted with 1% trifluoroacetic acid, desalted using C18 columns (Yingjie, OSPF0050-W), dried under vacuum, and stored at −80°C until LC–MS/MS analysis.

LC–MS/MS analysis and data processing

Eluted peptides were analyzed on a nanoElute 2 system coupled online to a timsTOF Pro2 mass spectrometer equipped with a CaptiveSpray ion source (Bruker Daltonics) and operated in data-dependent acquisition mode. Peptides were separated on a 25 cm × 75 µm analytical column packed in-house with 1.9 µm C18 PeproSil particles and maintained at 55°C. Mobile phase A consisted of 0.1% formic acid in water and mobile phase B consisted of 0.1% formic acid in acetonitrile. Peptides were eluted at a flow rate of 300 nL/min using a gradient from 2% to 80% B, including ramps of 2% to 32% B over 30 min, 32% to 40% B over 15 min, followed by two 5-min ramps to 60% and 80% B. The spray voltage was set to 1.5 kV, the mass range was 100–2000 m/z, and the ramp time was 200 ms. PASEF acquisition was performed with 6 MS/MS scans per cycle, a total cycle time of 1.44 s, an intensity threshold of 2500, and a target intensity of 20,000. Raw data were analyzed for peptide identification using PEAKS Studio, and peptide-spectrum visualization was performed using FragPipe-PDV.

Statistical analyses

Statistical analyses were performed by R or GraphPad Prism. Information on specific statistical tests is listed in the figure legends and/or method details. *P* values are listed in figures or figure legends. ns, not significant; * $P < 0.05$; ** $P < 0.01$; *** $P < 0.001$; **** $P < 0.0001$.

Results

Clonal expansion enriches reactive TCRs in a context-dependent manner but does not resolve reactivity strength

To directly test whether an expansion-based nomination strategy can effectively capture tumor reactivity in native tumors, we combined paired scTCR-seq, scRNA-seq, and clonotype-level functional validation of $CD8^+$ TILs isolated from the E0771 and LLC tumor models, reconstructing candidate clonotypes ranked by clone size (Fig. 1A and S1A, B). In E0771 $CD8^+$ TILs, we first prioritized the two most expanded paired clonotypes, E0-1 (clone size = 332) and E0-2 (clone size = 247), but both induced only weak CD69 upregulation in Jurkat–tumor co-culture assays (Fig. 1B, S1D). Upon extending the screen, we identified four reactive TCRs, E0-3 (153), E0-4 (19), E0-5 (8), and E0-6 (5), including low-frequency clonotypes that still showed clear tumor reactivity (Fig. 1C). A similar pattern was observed for LLC $CD8^+$ TIL-derived clonotypes: the two highly expanded clonotypes, LLC-1 (165) and LLC-2 (101), again showed only weak activation, whereas two reactive TCRs, LLC-3 (9) and LLC-4 (5), were identified from low-frequency clonotypes after expanding the screen (Fig. 1E, F). Scatterplot analysis further showed that CD69 induction did not exhibit a simple positive relationship with clonotype size among TCRs derived from E0771 or LLC $CD8^+$ TILs (Fig. 1D, G). Together, these data indicate that highly expanded clonotypes do not reliably correspond to the strongest functional responses in native $CD8^+$ TIL compartments, and that bona fide reactive TCRs can also reside in low-frequency clones.

Because clonal expansion alone did not explain the functional differences observed among clonotypes recovered from native $CD8^+$ TILs, we next sought to examine more proximal variables underlying tumor-cell recognition in an antigen-defined setting. For a given reactive TCR, signal 1 can be resolved into at least two experimentally separable components: the functional avidity of the TCR for its cognate peptide–MHC complex and the abundance of that peptide's presentation on tumor cells. A direct comparison of these variables requires that TCR specificity, peptide

presentation abundance, and TCR avidity be defined within the same system, which is difficult to achieve comprehensively for reactive TCRs recovered from native tumors. We therefore turned to the MB49-OVA model for joint analysis of these two dimensions of signal 1.

We first asked how informative clone size remained in this model. From a total of 777 paired clonotypes recovered from MB49-OVA CD8$^+$ TILs, we selected the top 17 expanded clonotypes for reconstruction and functional testing. Sixteen of these 17 clonotypes induced clear CD69 upregulation upon co-culture with MB49-OVA tumor cells, whereas only one was classified as non-reactive (Fig. 1H and S1C, E-G). The validated reactive clonotypes spanned a broad range of clone sizes, from 86 to 784, and their CD69 responses also varied substantially across the set (Fig. 1H, I). Notably, strong tumor-cell recognition was not restricted to the largest MB49-OVA CD8$^+$ TIL-derived clonotypes. Several clonotypes with intermediate or relatively low frequencies still induced robust CD69 upregulation, whereas some of the most expanded clonotypes showed only moderate responses (Fig. 1I and S2A, B, E). Thus, in MB49-OVA CD8$^+$ TILs, clonal expansion efficiently enriched reactive TCRs, but did not by itself resolve the relative magnitude of reactivity within the reactive pool.

TCR avidity and peptide presentation jointly shape tumor recognition strength and state bias

To define the antigenic basis of the functional heterogeneity observed among MB49-OVA CD8$^+$ TIL-derived reactive clonotypes, we first profiled the peptide presentation landscape of MB49-OVA by MHC-I immunopeptidomics. Among the most abundant presented ligands, two OVA-derived peptides, SIINFEKL and KVVRFDKL, were prominently detected (Fig. 2A and S2C, D; Table S1). We then assigned the validated reactive clonotypes according to peptide specificity and divided them into a SIIN-reactive group and a KVV-reactive group. Based on peptide titration profiles, the SIIN-reactive clonotypes were further separated into a high-avidity SIIN_High group and a low-avidity SIIN_Low group (Fig. 2B, C). Within the expanded reactive set, these groups comprised eight SIIN_High clonotypes, three SIIN_Low clonotypes, and five KVV clonotypes, and all three groups contributed comparably to the reactive clonal pool in vivo (Fig. 2C and S1H). Importantly, these groups were not composed exclusively of highly expanded clonotypes; low-frequency reactive clonotypes were also represented within the SIIN_High and KVV groups (Figure S2E-G). Peptide titration assays established a clear hierarchy of functional avidity across the three groups: SIIN_High TCRs showed the greatest peptide sensitivity, SIIN_Low TCRs showed the lowest, and KVV TCRs were intermediate (Fig. 2B–D). The groupwise -log10(EC50) values ranged from 9.2 to 10.6 for SIIN_High, 7.2 to 7.3 for SIIN_Low, and 8.2 to 9.0 for KVV (Fig. 2C, D). Notably, even within the SIINFEKL-specific subset, clonotype size was not strongly coupled to functional avidity (Fig. 2E).

We next asked whether this avidity hierarchy was preserved when the same TCRs encountered intact tumor cells. This was not the case. In peptide titration assays, KVV TCRs were more sensitive than SIIN_Low TCRs (Fig. 2B–D). However, when co-cultured with MB49-OVA tumor cells, SIIN_Low TCRs induced stronger CD69 responses than KVV TCRs (Fig. 2F). Accordingly, the groupwise tumor-cell recognition output ranked as SIIN_High > SIIN_Low > KVV, which differed from the ordering inferred from peptide sensitivity alone (Fig. 2D, F). This reversal was consistent with the difference in tumor-side peptide availability, because SIINFEKL was detected at higher abundance than KVVRFDKL in the immunopeptidomics analysis (Fig. 2A). Thus, peptide titration–based avidity ranking did not directly match the ranking of tumor-cell recognition in the tumor-cell context.

We then mapped the 16 functionally validated reactive TCRs back onto the single-cell atlas of MB49-OVA CD8$^+$ TILs to examine whether these differences were also associated with distinct in vivo state distributions. Reactive cells were broadly distributed across the atlas rather than confined to a single transcriptional compartment (Fig. 2G and S2H, I). When analyzed by TCR group, distinct state biases became apparent. SIIN_High cells were concentrated in Teff_inflam, SIIN_Low cells preferentially localized to Teff_cytotox with partial extension toward other states, whereas KVV cells were enriched in Cycl_CD8 and Teff_Cxcr6 and showed elevated *Gzmk*, *Cxcr6*, and *Mki67* (Fig. 2H-J). Within SIINFEKL-specific cells, SIIN_High and SIIN_Low further differed in effector gene modules: SIIN_High displayed higher expression of *Ifng* and inflammatory chemokines (*Ccl3* and *Ccl4*), whereas SIIN_Low showed higher *Gzma* and *Gzmk*. Notably, SIIN_High and KVV TCRs identified among low-frequency reactive clonotypes also showed atlas distribution patterns broadly similar to those of the corresponding expanded groups (Figure S2J-M). Together, these data indicate that reactive TCRs with different combinations of TCR avidity and peptide presentation show different in vivo state distributions in addition to differences in acute tumor-cell recognition.

In the MB49-OVA model, in addition to OVA-reactive TCRs, we also identified a subset of TCRs reactive to parental MB49 antigens. Unlike the OVA-reactive groups described above, these MB49-reactive TCRs showed a distinct distribution across the transcriptional atlas, occupying less activated states. By contrast, MB49-reactive TCRs identified in parental MB49 tumors displayed a more effector-biased distribution together with greater clonal expansion (Fig. S3A-E). Notably, Jurkat cells transduced with MB49-reactive TCRs derived from either MB49-OVA or parental MB49 recognized MB49 tumor cells with comparable CD69 induction in vitro (Fig. S3F). These findings suggest that, in the MB49-OVA model, MB49-reactive clonotypes retain intrinsic tumor-recognition capacity, whereas their limited in vivo expansion and less effector-biased states may reflect competition from dominant OVA-reactive clonotypes (Fig. S3G). Together, these observations highlight tumor context as an additional layer shaping the in vivo state distribution of reactive clonotypes beyond their intrinsic recognition capacity.

Discussion

Our study supports the view that clonal expansion is informative (6, 8), but should not be regarded as a stable indicator for tumor reactivity in native tumors. In both E0771 and LLC, highly expanded clonotypes did not consistently correspond to the strongest functional responses, whereas clear tumor reactivity was also observed among low-frequency clones. These findings argue that low-frequency clonotypes should not be overlooked during the nomination of tumor-reactive TCRs. This pattern is not unexpected in tumors, where reactive clonotypes are likely to undergo repeated cycles of stimulation, expansion, contraction and tissue retention (10). Single-cell atlases capture only one time point within this dynamic process, whereas the observed expansion state reflects its cumulative outcome rather than an instantaneous measurement of tumor recognition strength. Accordingly, clone size may provide a useful clue for candidate enrichment, but not a direct estimate of ongoing tumor-reactive output.

These observations point to a more direct question: if clone size itself is insufficient to explain functional differences among reactive TCRs, what variables more proximally constrain tumor-cell recognition? Among the reactive TCRs identified in MB49-OVA, the avidity hierarchy established by peptide titration was not preserved when the same TCRs encountered intact tumor cells. Instead,

differences in tumor-side peptide abundance were sufficient to reorder the relative performance of reactive TCRs. This suggests that, in the tumor-cell context, avidity measured under conditions of saturating peptide presentation is not sufficient to rank the strength of TCR reactivity against tumor cells. From this perspective, so-called optimal avidity is better viewed as a conditional property that depends on the presentation landscape in which a given TCR is evaluated, rather than as a fixed intrinsic attribute of the TCR itself.

In MB49-OVA CD8$^+$ TILs, reactive TCRs spanning different combinations of TCR avidity and peptide presentation were all capable of giving rise to expanded clonotypes in vivo, and the differences in clone size among them were not always pronounced. For example, even among SIINFEKL-specific TCRs, for which antigen abundance should in principle be comparable, both the high-avidity and low-avidity groups contained TCRs that were either strongly expanded or only weakly expanded. This implies that once antigenic input exceeds a certain level, TCRs above a minimum avidity threshold may all be sufficient to drive expansion. By contrast, these groups displayed reproducible biases in their distributions across the single-cell atlas. Specifically, SIIN_High, SIIN_Low and KVV TCRs each preferentially occupied distinct transcriptional compartments, indicating that different combinations of TCR avidity and peptide presentation are associated with different state distributions. Thus, differences in signal-1 composition may not necessarily be reflected in a sustained separation of clone size, but may instead emerge as biased transcriptional programs and state preferences among reactive T cells.

MB49-OVA represents a relatively strong and controllable antigenic setting, whereas native tumors are more likely to contain antigen landscapes of lower abundance, greater heterogeneity and ongoing dynamic remodeling (15, 20). In addition, clonotypes directed against different tumor antigens may compete with one another (21, 22). When one antigen elicits broad and strong clonal expansion, other reactive clonotypes may fail to gain opportunities for expansion even if they retain substantial recognition capacity. We therefore regard the present study as a concrete example of how avidity and presentation cooperate to shape the TCR repertoire, rather than as a universal rule for ranking tumor-reactive TCRs. Within this framework, antigen abundance, TCR avidity and clonal competition jointly shape clonal expansion, indicating that highly expanded clonotypes alone may not fully capture the functional breadth of tumor-reactive repertoires. This consideration is particularly relevant for candidate nomination, where low-frequency clonotypes may represent an underexplored source of functionally valuable tumor-reactive TCRs. Importantly, our results also show how strongly OVA overexpression can inflate antigen abundance and drive clonal expansion. Conclusions drawn from OVA-based immune models may therefore, at least in part, reflect a simplified experimental regime rather than the full complexity of clonal dynamics and epitope competition in real tumors.

Acknowledgments

We thank Singleron Biotechnologies for sequencing-related technical support.
This work was supported by the National Natural Science Foundation of China (T2525022, 22588302, and 32450763), the National Key Research and Development Program of China (2023YFA1506500), the Natural Science Foundation of Jiangsu Province (BK20240007 and BK20232020), and the Yachen Funding for Innovation.

Author contributions: J.P. Li and S. Ouyang conceived and designed the study and wrote the manuscript; Z. Zhao, S. Liu, S. Ma, X. Wu, M. Fan, and N. Jiang performed research; S. Liu performed omics mass spectrometry experiments and analyses; Z. Zhao and N. Jiang isolated TILs; X. Wu assisted with single-cell sequencing analysis; S. Ma and M. Fan assisted with TCR-Jurkat construction and functional validation; S. Ouyang prepared the figures; and all authors analyzed data and reviewed the manuscript.

Disclosures: The authors declare no competing financial interests.

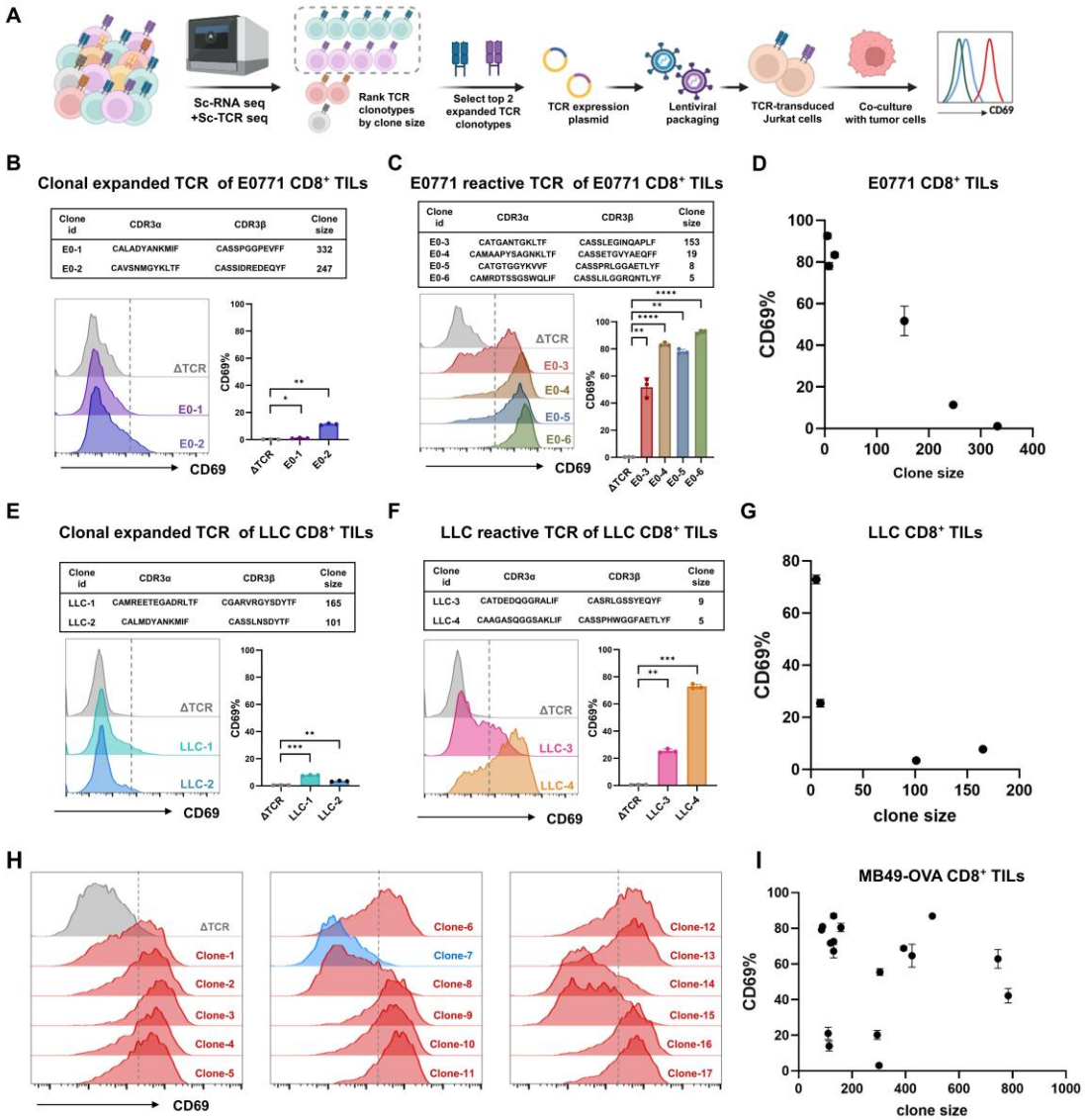

Figure 1. Clonal expansion enriches reactive TCRs in a context-dependent manner but does not resolve reactivity strength

(A) Overview of the integrated workflow and functional validation. MB49-OVA CD8$^+$ TILs were profiled by scRNA-seq and paired scTCR-seq to define transcriptional states and recover full-length TCR sequences. Paired TCR clonotypes were ranked by clonotype size and defined by identical matched TCRα and TCRβ sequences. Selected full-length TCRs were reconstructed, packaged into lentivirus, and expressed in ΔTCR Jurkat cells (TCR-deficient Jurkat cells). TCR-transduced Jurkat cells were co-cultured with MB49-OVA cells at a 1:2 ratio (Jurkat:tumor) for 18 h, and CD69 induction was measured by flow cytometry.

(B and E) Top expanded clonotypes from E0771 CD8$^+$ TILs (B) and LLC CD8$^+$ TILs (E). Tables (top) list the two most expanded paired clonotypes, including paired CDR3α/CDR3β sequences and clonotype sizes. Flow cytometry histograms (bottom left) show CD69 after tumor co-culture for ΔTCR (gray) and the indicated TCR-transduced Jurkat cells. Bar plots (bottom right) quantify CD69$^+$ frequency. Data are shown as mean ± SEM from n = 3 independent co-culture experiments per group. *P* values were calculated by two-sided unpaired t tests for the indicated comparisons. Significance levels are indicated in the plots.

(C and F) Functionally validated tumor-reactive clonotypes from E0771 $CD8^+$ TILs (C) and LLC $CD8^+$ TILs (F). Tables (top) list validated reactive TCRs with paired CDR3α/CDR3β sequences and clonotype sizes. Flow cytometry histograms (bottom left) show CD69 after tumor co-culture for ΔTCR (gray) and the indicated TCR-transduced Jurkat cells. Bar plots (bottom right) quantify $CD69^+$ frequency. Data are shown as mean ± SEM from n = 3 independent co-culture experiments per group. *P* values were calculated by two-sided unpaired t tests for the indicated comparisons. Significance levels are indicated in the plots.

(D and G) Relationship between clonotype size and functional tumor reactivity of validated TCRs derived from E0771 $CD8^+$ TILs (D) and LLC $CD8^+$ TILs (G). Each dot represents one validated clonotype, plotted by clonotype size and the frequency of $CD69^+$ Jurkat cells after tumor co-culture.

(H) Representative flow cytometry histograms showing CD69 induction in TCR-transduced Jurkat cells after co-culture with MB49-OVA tumor cells. ΔTCR Jurkat cells served as the negative control (gray). Reactive and non-reactive clonotypes are shown in red and blue, respectively. Reactivity was defined as $CD69^+ \geq 10\%$.

(I) Relationship between clonotype size and functional tumor reactivity among the top expanded clonotypes recovered from MB49-OVA $CD8^+$ TILs. Each dot represents one reconstructed clonotype, plotted by clonotype size and the frequency of $CD69^+$ Jurkat cells after co-culture with MB49-OVA tumor cells.

Parts A was created using BioRender.

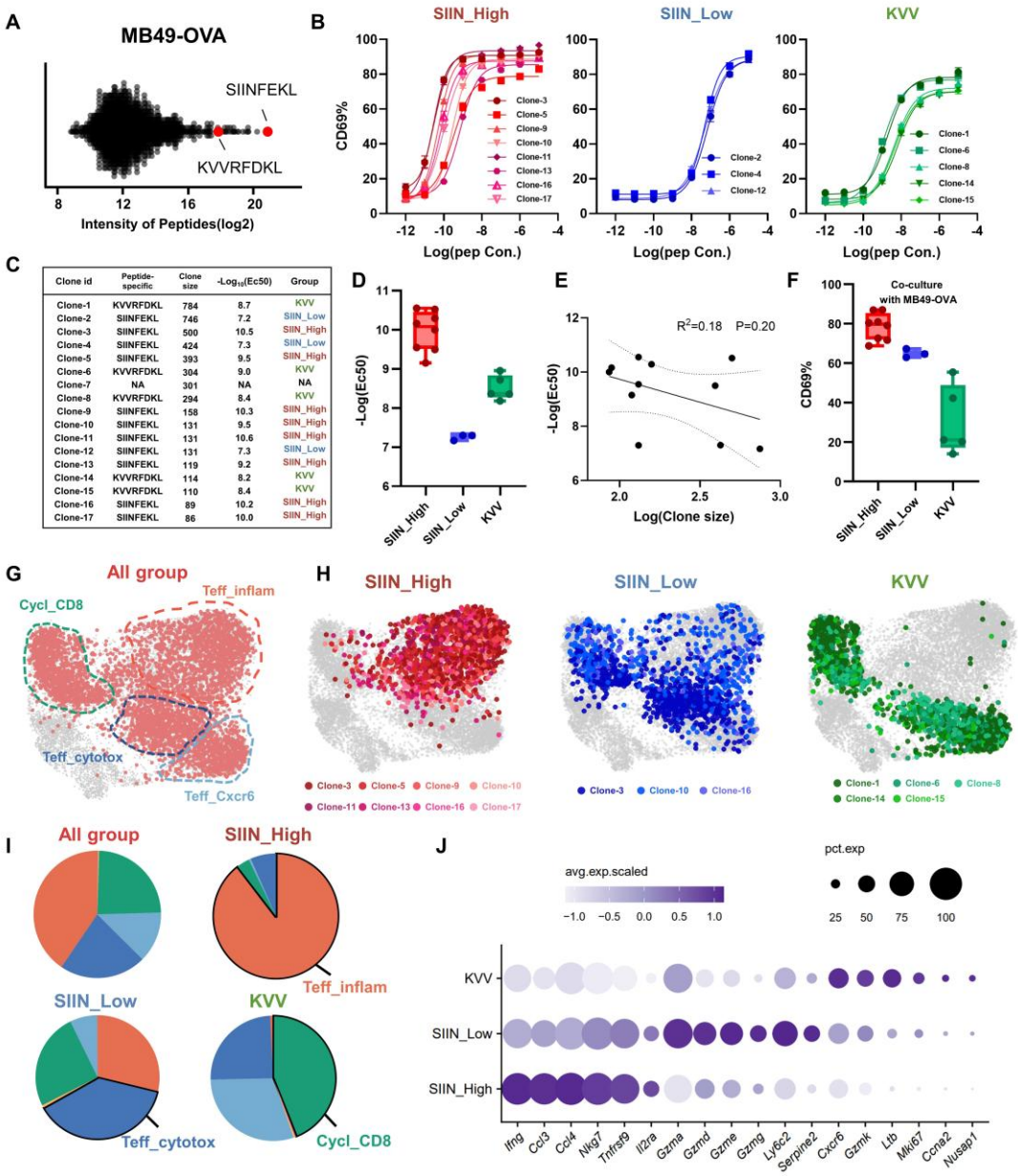

Clone id	Peptide-specific	Clone size	-Log$_{10}$(Ec50)	Group
Clone-1	KVVRFDKL	784	8.7	KVV
Clone-2	SIINFEKL	746	7.2	SIIN_Low
Clone-3	SIINFEKL	500	10.5	SIIN_High
Clone-4	SIINFEKL	424	7.3	SIIN_Low
Clone-5	SIINFEKL	393	9.5	SIIN_High
Clone-6	KVVRFDKL	304	9.0	KVV
Clone-7	NA	301	NA	NA
Clone-8	KVVRFDKL	294	8.4	KVV
Clone-9	SIINFEKL	158	10.3	SIIN_High
Clone-10	SIINFEKL	131	9.5	SIIN_High
Clone-11	SIINFEKL	131	10.6	SIIN_High
Clone-12	SIINFEKL	131	7.3	SIIN_Low
Clone-13	SIINFEKL	119	9.2	SIIN_High
Clone-14	KVVRFDKL	114	8.2	KVV
Clone-15	KVVRFDKL	110	8.4	KVV
Clone-16	SIINFEKL	89	10.2	SIIN_High
Clone-17	SIINFEKL	86	10.0	SIIN_High

Figure 2. Avidity and peptide presentation jointly shape tumor recognition strength and state bias

(A) Peptide intensity distribution (log2) from MHC class I immunopeptidomics of MB49-OVA tumor cells. Each point represents one identified peptide. SIINFEKL and KVVRFDKL are highlighted in red.

(B) Peptide titration curves for TCR-transduced Jurkat cells co-cultured with H-2K^{b}-expressing MC38 cells at a 1:1 ratio for 18 h in the presence of serially diluted SIINFEKL or KVVRFDKL peptide (10^{-12} to 10^{-5} M). CD69 induction was quantified as CD69^{+} frequency, and EC50 values were derived from dose-response curves. Data are shown as mean ± SEM from n = 3 independent peptide-stimulation experiments for each TCR.

(C) Table summarizing reactive TCR clonotypes, including peptide specificity (SIINFEKL or KVVRFDKL), clonotype size, functional avidity (-log$_{10}$(EC50)), and group assignment. SIIN_High and SIIN_Low denote SIINFEKL-specific TCRs with higher and lower functional

avidity, respectively; KVV denotes KVVRFDKL-specific TCRs.

(D) Box plot summarizing functional avidity ($-\log_{10}$(EC50)) across SIIN_High (n=8), SIIN_Low (n=3), and KVV groups (n=5); each point represents one TCR.

(E) Correlation between clonotype size and functional avidity ($-\log_{10}$(EC50)) for SIINFEKL-specific TCRs. Each point represents one SIINFEKL-specific TCR clonotype. The relationship was assessed by simple linear regression; the solid line indicates the fitted regression line and dotted lines indicate the 95% confidence interval. R^2 and *P* value are shown in the plot.

(F) Box plot showing the percentage of $CD69^+$ cells among TCR-transduced Jurkat cells after co-culture with MB49-OVA tumor cells. Each point represents one TCR clonotype, and values are shown as the mean $CD69^+$ frequency from n = 3 independent co-culture experiments. SIIN_High (n=8), SIIN_Low (n=3), and KVV groups (n=5).

(G) UMAP of MB49-OVA $CD8^+$ TILs scRNA-seq data with cells from all validated MB49-OVA reactive clonotypes pooled (All group) highlighted.

(H) UMAP projections highlighting reactive clonotypes from each group (SIIN_High, SIIN_Low, KVV). Colors denote individual clonotypes and other cells are shown in gray.

(I) Pie charts showing the transcriptional subset composition of reactive cells for All group and for each TCR group (SIIN_High, SIIN_Low, KVV). The dominant subset is annotated.

(J) Dot plot summarizing expression of selected marker genes across SIIN_High, SIIN_Low, and KVV groups. Dot color indicates scaled average expression and dot size indicates the fraction of expressing cells.

Reference

1. Tran, E., P. F. Robbins, Y.-C. Lu, T. D. Prickett, J. J. Gartner, L. Jia, A. Pasetto, Z. Zheng, S. Ray, E. M. Groh, I. R. Kriley, and S. A. Rosenberg. 2016. T-Cell Transfer Therapy Targeting Mutant KRAS in Cancer. *N Engl J Med* 375: 2255–2262.

2. Leidner, R., N. Sanjuan Silva, H. Huang, D. Sprott, C. Zheng, Y.-P. Shih, A. Leung, R. Payne, K. Sutcliffe, J. Cramer, S. A. Rosenberg, B. A. Fox, W. J. Urba, and E. Tran. 2022. Neoantigen T-Cell Receptor Gene Therapy in Pancreatic Cancer. *N Engl J Med* 386: 2112–2119.

3. Caushi, J. X., J. Zhang, Z. Ji, A. Vaghasia, B. Zhang, E. H.-C. Hsiue, B. J. Mog, W. Hou, S. Justesen, R. Blosser, A. Tam, V. Anagnostou, T. R. Cottrell, H. Guo, H. Y. Chan, D. Singh, S. Thapa, A. G. Dykema, P. Burman, B. Choudhury, L. Aparicio, L. S. Cheung, M. Lanis, Z. Belcaid, M. El Asmar, P. B. Illei, R. Wang, J. Meyers, K. Schuebel, A. Gupta, A. Skaist, S. Wheelan, J. Naidoo, K. A. Marrone, M. Brock, J. Ha, E. L. Bush, B. J. Park, M. Bott, D. R. Jones, J. E. Reuss, V. E. Velculescu, J. E. Chaft, K. W. Kinzler, S. Zhou, B. Vogelstein, J. M. Taube, M. D. Hellmann, J. R. Brahmer, T. Merghoub, P. M. Forde, S. Yegnasubramanian, H. Ji, D. M. Pardoll, and K. N. Smith. 2021. Transcriptional programs of neoantigen-specific TIL in anti-PD-1-treated lung cancers. *Nature* 596: 126–132.

4. Oliveira, G., K. Stromhaug, S. Klaeger, T. Kula, D. T. Frederick, P. M. Le, J. Forman, T. Huang, S. Li, W. Zhang, Q. Xu, N. Cieri, K. R. Clauser, S. A. Shukla, D. Neuberg, S. Justesen, G. MacBeath, S. A. Carr, E. F. Fritsch, N. Hacohen, M. Sade-Feldman, K. J. Livak, G. M. Boland, P. A. Ott, D. B. Keskin, and C. J. Wu. 2021. Phenotype, specificity and avidity of antitumour CD8+ T cells in melanoma. *Nature* 596: 119–125.

5. Lowery, F. J., S. Krishna, R. Yossef, N. B. Parikh, P. D. Chatani, N. Zacharakis, M. R. Parkhurst, N. Levin, S. Sindiri, A. Sachs, K. J. Hitscherich, Z. Yu, N. R. Vale, Y.-C. Lu, Z. Zheng, L. Jia, J. J. Gartner, V. K. Hill, A. R. Copeland, S. K. Nah, R. V. Masi, B. Gasmi, S. Kivitz, B. C. Paria, M. Florentin, S. P. Kim, K. Hanada, Y. F. Li, L. T. Ngo, S. Ray, M. L. Shindorf, S. T. Levi, R. Shepherd, C. Toy, A. Y. Parikh, T. D. Prickett, M. C. Kelly, R. Beyer, S. L. Goff, J. C. Yang, P. F. Robbins, and S. A. Rosenberg. 2022. Molecular signatures of antitumor neoantigen-reactive T cells from metastatic human cancers. *Science* 375: 877–884.

6. Pasetto, A., A. Gros, P. F. Robbins, D. C. Deniger, T. D. Prickett, R. Matus-Nicodemos, D. C. Douek, B. Howie, H. Robins, M. R. Parkhurst, J. Gartner, K. Trebska-McGowan, J. S. Crystal, and S. A. Rosenberg. 2016. Tumor- and Neoantigen-Reactive T-cell Receptors Can Be Identified Based on Their Frequency in Fresh Tumor. *Cancer Immunol Res* 4: 734–743.

7. Gros, A., P. F. Robbins, X. Yao, Y. F. Li, S. Turcotte, E. Tran, J. R. Wunderlich, A. Mixon, S. Farid, M. E. Dudley, K.-I. Hanada, J. R. Almeida, S. Darko, D. C. Douek, J. C. Yang, and S. A. Rosenberg. 2014. PD-1 identifies the patient-specific CD8+tumor-reactive repertoire infiltrating human tumors. *J Clin Invest* 124: 2246–2259.

8. Hanada, K., C. Zhao, R. Gil-Hoyos, J. J. Gartner, C. Chow-Parmer, F. J. Lowery, S. Krishna, T. D. Prickett, S. Kivitz, M. R. Parkhurst, N. Wong, Z. Rae, M. C. Kelly, S. L. Goff, P. F. Robbins, S. A. Rosenberg, and J. C. Yang. 2022. A phenotypic signature that identifies neoantigen-reactive T cells in fresh human lung cancers. *Cancer Cell* 40: 479-493.e6.

9. Simoni, Y., E. Becht, M. Fehlings, C. Y. Loh, S.-L. Koo, K. W. W. Teng, J. P. S. Yeong, R. Nahar, T. Zhang, H. Kared, K. Duan, N. Ang, M. Poidinger, Y. Y. Lee, A. Larbi, A. J. Khng, E. Tan, C. Fu, R. Mathew, M. Teo, W. T. Lim, C. K. Toh, B.-H. Ong, T. Koh, A. M. Hillmer, A. Takano, T. K. H.

Lim, E. H. Tan, W. Zhai, D. S. W. Tan, I. B. Tan, and E. W. Newell. 2018. Bystander CD8(+) T cells are abundant and phenotypically distinct in human tumour infiltrates. *Nature* 557: 575–579.

10. Chiffelle, J., D. Barras, R. Pétremand, A. Orcurto, S. Bobisse, M. Arnaud, A. Auger, B. N. Rodrigo, E. Ghisoni, C. Sauvage, D. Saugy, A. Michel, B. Murgues, N. Fahr, M. Imbimbo, M. Ochoa de Olza, S. Latifyan, I. Crespo, F. Benedetti, R. Genolet, L. Queiroz, J. Schmidt, K. Homicsko, S. Zimmermann, O. Michielin, M. Bassani-Sternberg, L. E. Kandalaft, U. Dafni, J. Corria-Osorio, L. Trueb, D. Dangaj Laniti, A. Harari, and G. Coukos. 2024. Tumor-reactive T cell clonotype dynamics underlying clinical response to TIL therapy in melanoma. *Immunity* 57: 2466-2482.e12.

11. Morgan, D. M., B. L. Horton, V. Bhandarkar, R. Van, T. Dinter, M. Zagorulya, J. C. Love, and S. Spranger. 2024. Expansion of tumor-reactive CD8(+) T cell clonotypes occurs in the spleen in response to immune checkpoint blockade. *Sci Immunol* 9: eadi3487.

12. Smith-Garvin, J. E., G. A. Koretzky, and M. S. Jordan. 2009. T cell activation. *Annu Rev Immunol* 27: 591–619.

13. Holler, P. D., and D. M. Kranz. 2003. Quantitative analysis of the contribution of TCR/pepMHC affinity and CD8 to T cell activation. *Immunity* 18: 255–264.

14. González, P. A., L. J. Carreño, D. Coombs, J. E. Mora, E. Palmieri, B. Goldstein, S. G. Nathenson, and A. M. Kalergis. 2005. T cell receptor binding kinetics required for T cell activation depend on the density of cognate ligand on the antigen-presenting cell. *Proc Natl Acad Sci U S A* 102: 4824–4829.

15. Kalaora, S., Y. Wolf, T. Feferman, E. Barnea, E. Greenstein, D. Reshef, I. Tirosh, A. Reuben, S. Patkar, R. Levy, J. Quinkhardt, T. Omokoko, N. Qutob, O. Golani, J. Zhang, X. Mao, X. Song, C. Bernatchez, C. Haymaker, M.-A. Forget, C. Creasy, P. Greenberg, B. W. Carter, Z. A. Cooper, S. A. Rosenberg, M. Lotem, U. Sahin, G. Shakhar, E. Ruppin, J. A. Wargo, N. Friedman, A. Admon, and Y. Samuels. 2018. Combined Analysis of Antigen Presentation and T-cell Recognition Reveals Restricted Immune Responses in Melanoma. *Cancer Discov* 8: 1366–1375.

16. Liu, Z., J. P. Li, M. Chen, M. Wu, Y. Shi, W. Li, J. R. Teijaro, and P. Wu. 2020. Detecting Tumor Antigen-Specific T Cells via Interaction-Dependent Fucosyl-Biotinylation. *Cell* 183: 1117-1133.e19.

17. Qiu, S., W. Li, T. Deng, A. Bi, Y. Yang, X. Jiang, and J. P. Li. 2023. Ru(bpy)32+-Enabled Cell-Surface Photocatalytic Proximity Labeling toward More Efficient Capture of Physically Interacting Cells. *Angew Chem Int Ed* e202303014.

18. Liu, H., H. Luo, Q. Xue, S. Qin, S. Qiu, S. Liu, J. Lin, J. P. Li, and P. R. Chen. 2022. Antigen-Specific T Cell Detection via Photocatalytic Proximity Cell Labeling (PhoXCELL). *J. Am. Chem. Soc.* 144: 5517–5526.

19. Deng, T., X. Jiang, Z. Zhao, X. Zhao, A. Bi, S. Ouyang, S. Sun, S. Qiu, M. Fan, Q. Xue, W. Yu, Y. Yang, W. Li, Y. Wu, X. Huang, D. Zhong, S. Qin, W. Zhu, and J. P. Li. 2025. CINTER-seq: Chemical profiling reveals interaction-dependent cell landscapes and gene signatures in vivo. *Immunity* 58: 2336-2352.e12.

20. Yadav, M., S. Jhunjhunwala, Q. T. Phung, P. Lupardus, J. Tanguay, S. Bumbaca, C. Franci, T. K. Cheung, J. Fritsche, T. Weinschenk, Z. Modrusan, I. Mellman, J. R. Lill, and L. Delamarre. 2014. Predicting immunogenic tumour mutations by combining mass spectrometry and exome sequencing. *Nature* 515: 572–576.

21. Kedl, R. M., W. A. Rees, D. A. Hildeman, B. Schaefer, T. Mitchell, J. Kappler, and P. Marrack.

549 2000. T cells compete for access to antigen-bearing antigen-presenting cells. *J Exp Med* 192: 1105–
550 1113.
551 22. Burger, M. L., A. M. Cruz, G. E. Crossland, G. Gaglia, C. C. Ritch, S. E. Blatt, A. Bhutkar, D.
552 Canner, T. Kienka, S. Z. Tavana, A. L. Barandiaran, A. Garmilla, J. M. Schenkel, M. Hillman, I. de
553 Los Rios Kobara, A. Li, A. M. Jaeger, W. L. Hwang, P. M. K. Westcott, M. P. Manos, M. M.
554 Holovatska, F. S. Hodi, A. Regev, S. Santagata, and T. Jacks. 2021. Antigen dominance hierarchies
555 shape TCF1(+) progenitor CD8 T cell phenotypes in tumors. *Cell* 184: 4996-5014.e26.
556